PHYSICAL REVIEW E **92**, 012108 (2015)

Nonlocal response functions for predicting shear flow of strongly inhomogeneous fluids. II. Sinusoidally driven shear and multisinusoidal inhomogeneity

Benjamin A. Dalton, Kirill S. Glavatskiy, and Peter J. Daivis
School of Applied Sciences, RMIT University, GPO Box 2476 Melbourne, Victoria 3001, Australia

B. D. Todd
Department of Mathematics, Faculty of Science, Engineering and Technology, and Centre for Molecular Simulation, Swinburne University of Technology, PO Box 218, Hawthorn, Victoria 3122, Australia

(Received 12 February 2015; revised manuscript received 29 April 2015; published 6 July 2015)

We use molecular-dynamics computer simulations to investigate the density, strain-rate, and shear-pressure responses of a simple model atomic fluid to transverse and longitudinal external forces. We have previously introduced a response function formalism for describing the density, strain-rate, and shear-pressure profiles in an atomic fluid when it is perturbed by a combination of longitudinal and transverse external forces that are independent of time and have a simple sinusoidal spatial variation. In this paper, we extend the application of the previously introduced formalism to consider the case of a longitudinal force composed of multiple sinusoidal components in combination with a single-component sinusoidal transverse force. We find that additional harmonics are excited in the density, strain-rate, and shear-pressure profiles due to couplings between the force components. By analyzing the density, strain-rate, and shear-pressure profiles in Fourier space, we are able to evaluate the Fourier coefficients of the response functions, which now have additional components describing the coupling relationships. Having evaluated the Fourier coefficients of the response functions, we are then able to accurately predict the density, velocity, and shear-pressure profiles for fluids that are under the influence of a longitudinal force composed of two or three sinusoidal components combined with a single-component sinusoidal transverse force. We also find that in the case of a multisinusoidal longitudinal force, it is sufficient to include only pairwise couplings between different longitudinal force components. This means that it is unnecessary to include couplings between three or more force components in the case of a longitudinal force composed of many Fourier components, and this paves the way for a highly accurate but tractable treatment of nonlocal transport phenomena in fluids with density and strain-rate inhomogeneities on the molecular length scale.

DOI: 10.1103/PhysRevE.92.012108 PACS number(s): 05.20.Jj, 05.60.Cd

I. INTRODUCTION

Nanofluidic flow has recently been the subject of intense interest because of its importance for emerging applications in biomolecular analysis, separation science, and energy conversion [1]. An important conclusion that has emerged from recent work in this field is that for a variety of reasons, the usual Navier-Stokes description of hydrodynamics begins to break down when it is applied to fluid flow through channels of width less than about 10 molecular diameters (3–5 nm). When Poisson-Boltzmann theory and the Navier-Stokes equations of hydrodynamics are used to predict the velocity profile for electrokinetic flow, poor agreement with simulation results is obtained for channels that are less than 3 nm wide [2,3]. This poor agreement has been attributed to the neglect of ionic and solvent packing effects in the interfacial region, and density-functional theory improves the agreement [3]. However, there are several other effects that may be equally significant and may also need to be included in an accurate theory of nanofluidic transport. These include the nonlocal relationship between the velocity and shear pressure [4], nonlocal coupling between the velocity field and the density profile [5], and coupling between the translational and rotational velocity fields for molecular fluids [6]. Considering the complex interplay of these different factors, it seems prudent to consider simpler cases in which each of the different effects can be studied in isolation.

It is well known that a dense fluid near a fluid-solid interface will exhibit a density profile with strong spatial oscillations within the region directly neighboring the solid wall. These effects have been well investigated using molecular-dynamics (MD) and Monte Carlo (MC) computer simulations [5,7–12], and they are present in all dense fluids, including aqueous systems [3]. The oscillations, which can be attributed to the effects of atomic and molecular planar packing parallel to the wall, decay in the direction normal to the wall. The spatial period of the density oscillations is of the order of a single atomic diameter, and the decay length of the oscillations is typically less than 5 atomic diameters. In the case of nanoconfinement where the channel width is less than 10 atomic diameters, these strong fluid density oscillations can extend across the entire channel. When a fluid is driven to flow along a nanochannel, it is known that these strong density oscillations influence the flow profiles [5,7,12]. This was most clearly illustrated by Travis and Gubbins [13], who showed that the streaming velocity profiles exhibit large oscillations, which are clearly aligned with the oscillations in the density profile. A theory of transport in strongly inhomogeneous fluids based on the generalized Enskog-like theory has been proposed by Pozhar and Gubbins [14]. This microscopic theory is, in principle, capable of predicting many features of transport in highly inhomogeneous fluids. However, it does not display the coupling of density, strain rate, and shear pressure in a physically transparent way. From this point of view, a more phenomenological, mesoscopic approach may be useful.

It is difficult to use a nanoconfined system to investigate the coupling relationships between the strong density inhomogeneities and flow profiles because of the complexity of the density profiles, which are a natural fluid response to the presence of the confining walls. In previous work, we have introduced a framework that allows us to investigate the coupling relationships between strong density inhomogeneities and flow profiles that avoids the introduction of fluid-solid interfaces [15,16]. Instead of confining the fluid in a nanochannel, we apply periodic external forces to an unconfined system to produce both periodic density inhomogeneity and periodic flow. We showed that we could reproduce many of the relevant characteristics of nanoconfined flow, such as the spatially oscillating velocity profiles due to density and velocity coupling. In these periodic systems, we have a high level of control over the shape, amplitude, and wavelength of the perturbations, and we can exploit the advantages of Fourier analysis. Although these simplified systems are highly idealized, they provide an excellent tool for investigating the coupling between density and velocity gradients.

In our most recent work [17], we introduced a formalism for describing shearing inhomogeneous fluids in terms of a truncated functional expansion, where the density, velocity gradients, and shearing pressure are represented as the response of a fluid to transverse and longitudinal external forces. We expressed the response formalism in terms of the external forces because the external forces are the independent input functions. The density and velocity, and hence the strain rate, are strongly coupled and thus they are not independent input functions. At lowest order, the effects of the transverse and longitudinal forces are independent. However, for larger values of the forces, the transverse force can generate density variations in addition to a velocity field, and likewise the longitudinal force can couple with the transverse force and modify the velocity field. We also described how we might evaluate inhomogeneous density-dependent viscosities that could be used in a local average density model. In this current work, we do not consider this model or other similar constitutive equations, but rather we continue our investigation with the external force response function formalism. We will return to discuss the local average density model in future work.

In our previous work [17], we introduced composite external forces consisting of a sinusoidal transverse force (STF) that produces shearing flow, and a sinusoidal longitudinal force (SLF) that produces density inhomogeneity. We only considered the case in which these forces were each composed of single Fourier components. In this paper, we investigate the effects of using multiple Fourier component SLFs in superposition. The reason for doing this is that the density inhomogeneity due to packing at the solid wall in real systems, such as the nanoconfined fluid, cannot be reproduced by only a single Fourier component external force. By superimposing two and three Fourier components in our SLFs, we can directly observe the effects of each component on the density profile and clearly isolate any coupling between the combined components. We will find that there is indeed very significant coupling between each pair of Fourier components of the longitudinal force, but we also see that triplet and higher-order couplings can be neglected. It is the major attraction of this periodic external force method that we are able to isolate such effects, which would otherwise be indiscernible. We can also isolate the effects of coupling between the multiple components of the SLF on the velocity and shear-pressure profiles. We will see that these effects are also significant, but the coupling is limited and manageable. The ability to isolate and observe the effects of multiple-component SLF superposition on the density, velocity, and shear-pressure profile will be very helpful in understanding strongly inhomogeneous flow in nanoconfined fluids where the density profiles are far more complex than those produced by single Fourier component longitudinal forces.

II. THEORETICAL BACKGROUND

A. Nonlocal response functions

In a previous publication [17], we showed that we can express the density, strain rate, and shear pressure as a response to an external body force $\mathbf{F}(y) = (F_x(y),\ F_y(y))$, where $F_x(y)$ is a transverse force that produces shearing flow and $F_y(y)$ is a longitudinal force that produces density inhomogeneities. It will be assumed that the transverse force remains weak, while the longitudinal force may be moderately strong. We showed that if the density response to this force is truncated at the second order, it can be written as

$$\begin{aligned}\rho(y) = \rho_0 &+ \int \chi_y^{(1)}(y-y')F_y(y')dy' \\ &+ \frac{1}{2}\int \chi_{yy}^{(2)}(y-y',y-y'')F_y(y')F_y(y'')dy'dy'' \\ &+ \frac{1}{2}\int \chi_{xx}^{(2)}(y-y',y-y'')F_x(y')F_x(y'')dy'dy'',\end{aligned} \tag{1}$$

where ρ_0 is the density of the homogeneous fluid, $\chi_y^{(1)}$ and $\chi_{yy}^{(2)}$ are the first- and second-order response functions relating density perturbations to the longitudinal force, and $\chi_{xx}^{(2)}$ is the second-order response function relating density perturbations to the transverse force.

We also showed that the strain rate can be written as

$$\begin{aligned}\dot{\gamma}(y) = &\int \xi_x^{(1)}(y-y')\,F_x(y')\,dy' \\ &+ \int \xi_{xy}^{(2)}(y-y',y-y'')\,F_x(y')F_y(y'')\,dy'dy'' \\ &+ \int \xi_{xyy}^{(3)}(y-y',y-y'',y-y''')\,F_x(y')F_y(y'') \\ &\times F_y(y''')\,dy'dy''dy''',\end{aligned} \tag{2}$$

where $\xi_x^{(1)}$, $\xi_{xy}^{(2)}$, and $\xi_{xyy}^{(3)}$ are first-, second-, and third-order strain-rate response functions. The strain rate is usually the property of interest when discussing shear flow. However, we will often present our results in terms of the velocity profiles, which are easier to visualize. The strain rate is given by the derivative of the steaming velocity $\dot{\gamma}(y) = du(y)/dy$. The shear pressure can be written in the same form as the strain rate, defining $\pi_x^{(1)}$, $\pi_{xy}^{(2)}$, and $\pi_{xyy}^{(3)}$ as the first-, second-, and third-order shear-pressure response functions.

The truncated functional expansion for the density given by Eq. (1) is a reformulation of the highly successful density-functional theory of inhomogeneous liquid structure. In our formulation, we empirically determine the response functions instead of postulating their approximate form [15]. The functional expansion of the strain rate, Eq. (2), and the corresponding one for the shear pressure are generalizations of the linear nonlocal constitutive equation that we previously used to successfully describe shear flow with short-wavelength oscillations in the strain rate [4]. These relations could also be expressed as gradient expansions, leading to a van der Waals–type theory of inhomogeneous fluids in the case of the density, and a Chapman-Enskog-type theory of transport. The integral formulations that we present here have the advantage that they do not require the summation of high-order gradient expansions that these approaches would require for strongly inhomogeneous fluids.

In this paper, we are concerned with the density, strain-rate, and shear-pressure response when the external body force is given by a single-component sinusoidal transverse force (STF) and a multicomponent sinusoidal longitudinal force (SLF). We will begin with the case of a two-component SLF, and we will then extend this treatment to develop a simplified approach for investigating the effects of three-component SLFs.

B. Two-component SLF

The single-component STF and two-component SLF external body force are represented by

$$\mathbf{F}(y) = \left(F_n^x \sin(k_n y),\ F_{m_1}^y \sin(k_{m_1} y) + F_{m_2}^y \sin(k_{m_2} y)\right), \quad (3)$$

where $k_n = 2n\pi/L_y$ is the wave number of the STF for any positive integer n, and k_{m_1} and k_{m_2} are the wave numbers for the two SLF components for any pair of positive integers m_1 and m_2.

The density, strain-rate, and shear-pressure profiles are periodic, so they can each be written as a Fourier series:

$$\rho(y) = \sum_{p=0}^{\infty} \rho_p \cos(k_p y), \quad \dot{\gamma}(y) = \sum_{p=1}^{\infty} \dot{\gamma}_p \cos(k_p y),$$
$$\Pi(y) = \sum_{p=1}^{\infty} \Pi_p \cos(k_p y). \quad (4)$$

Likewise, we can write the streaming velocity profile as a Fourier series $u(y) = \sum_{p=1}^{\infty} u_p \sin(k_p y)$, where $\dot{\gamma}_p = k_p u_p$. In [17], we described how the response functions defined by Eqs. (1) and (2) and the corresponding equation for the shear pressure can also be expressed as Fourier series. Substituting the Fourier series representations for the response functions from [17], as well as the force given in Eq. (3) and the corresponding Fourier series profiles, into Eqs. (1) and (2) and the corresponding equation for the shear pressure, we can take the Fourier transform of each equation and hence determine which Fourier components will be present in the density, strain rate, and shear pressure for a fluid perturbed by Eq. (3).

The αth Fourier coefficient of the density for a fluid under the influence of $\mathbf{F}(y)$ is given by

$$\begin{aligned}\rho_\alpha = {} & \rho_0 \delta_{\alpha,0} - \frac{L_y}{2} F_{m_1}^y \chi_{m_1}^y \delta_{\alpha,m_1} - \frac{L_y}{2} F_{m_2}^y \chi_{m_2}^y \delta_{\alpha,m_2} \\ & + \frac{L_y^2}{8} F_{m_1}^y F_{m_1}^y \chi_{m_1,m_1}^{yy} \delta_{\alpha,2m_1} + \frac{L_y^2}{8} F_{m_2}^y F_{m_2}^y \chi_{m_2,m_2}^{yy} \delta_{\alpha,2m_2} \\ & + \frac{L_y^2}{8} F_{m_1}^y F_{m_2}^y \chi_{m_1,m_2}^{yy-} \delta_{\alpha,|m_1-m_2|} \\ & + \frac{L_y^2}{8} F_{m_1}^y F_{m_2}^y \chi_{m_1,m_2}^{yy+} \delta_{\alpha,m_1+m_2} + \frac{L_y^2}{8} F_n^x F_n^x \chi_{n,n}^{xx} \delta_{\alpha,2n}, \quad (5)\end{aligned}$$

where $\delta_{\alpha\beta}$ is the Kronecker delta, and we note that repeated indices here do not imply summation. $\chi_{m_1}^y$ and $\chi_{m_2}^y$ are the Fourier coefficients of the linear density response function at wave numbers m_1 and m_2 corresponding to the two SLF components, χ_{m_1,m_1}^{yy} and χ_{m_2,m_2}^{yy} are the Fourier coefficients of the second-order density response function corresponding to each SLF component, and $\chi_{n,n}^{xx}$ is the Fourier coefficient of the second-order, shear-induced density response function corresponding to the STF. All of these quantities appear in the single-component response theory discussed in detail previously [17]. χ_{m_1,m_2}^{yy+} and χ_{m_1,m_2}^{yy-} represent the density responses due to coupling between the two SLF components. Each SLF component contributes linearly, so we refer to this response as the bilinear density response. We see that these bilinear density response components are only excited when two SLF components of different wave number are present simultaneously. For a given pair of $F_{m_1}^y$ and $F_{m_2}^y$, we can evaluate the two bilinear response Fourier coefficients by

$$\chi_{m_1,m_2}^{yy-} = \frac{8\rho_{|m_1-m_2|}}{L^2 F_{m_1}^y F_{m_2}^y}, \quad \chi_{m_1,m_2}^{yy+} = \frac{8\rho_{m_1+m_2}}{L^2 F_{m_1}^y F_{m_2}^y}. \quad (6)$$

The Fourier space representation of the strain rate in terms of $\mathbf{F}(y)$ is given by

$$\begin{aligned}\dot{\gamma}_\alpha = {} & -\frac{L_y}{2} F_1^x \xi_n^x \delta_{\alpha,n} + \frac{L_y^2}{8} F_n^x F_{m_1}^y \left[\xi_{n,m_1}^{xy-} \delta_{\alpha,|n-m_1|} + \xi_{n,m_1}^{xy+} \delta_{\alpha,n+m_1}\right] + \frac{L_y^2}{8} F_n^x F_{m_2}^y \left[\xi_{n,m_2}^{xy-} \delta_{\alpha,|n-m_2|} + \xi_{n,m_2}^{xy+} \delta_{\alpha,n+m_2}\right] \\ & + \frac{L_y^3}{32} F_n^x F_{m_1}^y F_{m_1}^y \left[\xi_{n,m_1,m_1}^{xyy-} \delta_{\alpha,|n-2m_1|} + \xi_{n,m_1,m_1}^{xyy0} \delta_{\alpha,n} + \xi_{n,m_1,m_1}^{xyy+} \delta_{\alpha,n+2m_1}\right] \\ & + \frac{L_y^3}{32} F_n^x F_{m_2}^y F_{m_2}^y \left[\xi_{n,m_2,m_2}^{xyy-} \delta_{\alpha,|n-2m_2|} + \xi_{n,m_2,m_2}^{xyy0} \delta_{\alpha,n} + \xi_{n,m_2,m_2}^{xyy+} \delta_{\alpha,n+2m_2}\right] \\ & + \frac{L_y^3}{32} F_n^x F_{m_1}^y F_{m_2}^y \left[\xi_{n,m_1,m_2}^{xyy-+} \delta_{\alpha,|n-(m_1+m_2)|} + \xi_{n,m_1,m_2}^{xyy--} \delta_{\alpha,|n-|m_1-m_2||} + \xi_{n,m_1,m_2}^{xyy+-} \delta_{\alpha,n+|m_1-m_2|} + \xi_{n,m_1,m_2}^{xyy++} \delta_{\alpha,n+(m_1+m_2)}\right], \quad (7)\end{aligned}$$

and the shear pressure is given by

$$\begin{aligned}\Pi_\alpha =& -\frac{L_y}{2}F_n^x\pi_n^x\delta_{\alpha,n} + \frac{L_y^2}{8}F_n^xF_{m_1}^y\left[\pi_{n,m_1}^{xy-}\delta_{\alpha,|n-m_1|} + \pi_{n,m_1}^{xy+}\delta_{\alpha,n+m_1}\right] + \frac{L_y^2}{8}F_n^xF_{m_2}^y\left[\pi_{n,m_2}^{xy-}\delta_{\alpha,|n-m_2|} + \pi_{n,m_2}^{xy+}\delta_{\alpha,n+m_2}\right]\\ &+ \frac{L_y^3}{32}F_n^xF_{m_1}^yF_{m_1}^y\left[\pi_{n,m_1,m_1}^{xyy-}\delta_{\alpha,|n-2m_1|} + \pi_{n,m_1,m_1}^{xyy+}\delta_{\alpha,n+2m_1}\right] + \frac{L_y^3}{32}F_n^xF_{m_2}^yF_{m_2}^y\left[\pi_{n,m_2,m_2}^{xyy-}\delta_{\alpha,|n-2m_2|} + \pi_{n,m_2,m_2}^{xyy+}\delta_{\alpha,n+2m_2}\right]\\ &+ \frac{L_y^3}{32}F_n^xF_{m_1}^yF_{m_2}^y\left[\pi_{n,m_1,m_2}^{xyy-+}\delta_{\alpha,|n-(m_1+m_2)|} + \pi_{n,m_1,m_2}^{xyy--}\delta_{\alpha,|n-|m_1-m_2||} + \pi_{n,m_1,m_2}^{xyy+-}\delta_{\alpha,n+|m_1-m_2|} + \pi_{n,m_1,m_2}^{xyy++}\delta_{\alpha,n+(m_1+m_2)}\right].\end{aligned} \tag{8}$$

ξ_n^x and π_n^x are the Fourier coefficients for the linear response of the strain rate and shear pressure to the STF, $\xi_{n,m_1}^{xy\pm}$ and $\xi_{n,m_2}^{xy\pm}$ are the Fourier coefficients for the bilinear response of the strain rate to the coupled STF and SLF, and $\pi_{n,m_1}^{xy\pm}$ and $\pi_{n,m_2}^{xy\pm}$ are the Fourier coefficients for the bilinear response of the shear pressure. $\xi_{n,m_1,m_1}^{xyy\pm}$, $\xi_{n,m_2,m_2}^{xyy\pm}$, ξ_{n,m_1,m_1}^{xyy0}, and ξ_{n,m_2,m_2}^{xyy0} are the third-order strain-rate response coefficients that are linear in the STF and quadratic in the SLF, and $\pi_{n,m_1,m_1}^{xyy\pm}$ and $\pi_{n,m_2,m_2}^{xyy\pm}$ are the third-order shear-pressure response coefficients that are linear in the STF and quadratic in the SLF. All of these quantities are described in [17], where we also show that $\pi_{n,m_1,m_1}^{xyy0} = 0$ and $\pi_{n,m_2,m_2}^{xyy0} = 0$.

$\xi_{n,m_1,m_2}^{xyy\pm\pm}$ and $\pi_{n,m_1,m_2}^{xyy\pm\pm}$ represent the strain-rate and shear-pressure responses that are linear in the STF and each of the SLF components. For a combination of a single-component STF and a two-component SLF, we excite four additional harmonics in both the strain-rate and shear-pressure profiles. We refer to this as the trilinear response since each force component contributes linearly. For any F_n^x and any pair of $F_{m_1}^y$ and $F_{m_2}^y$ we can calculate the four trilinear strain-rate response coefficients from

$$\begin{aligned}\xi_{n,m_1,m_2}^{xyy++} &= \frac{32\dot\gamma_{n+(m_1+m_2)}}{L^3F_n^xF_{m_1}^yF_{m_2}^y}, & \xi_{n,m_1,m_2}^{xyy+-} &= \frac{32\dot\gamma_{|n+|m_1-m_2||}}{L^3F_n^xF_{m_1}^yF_{m_2}^y},\\ \xi_{n,m_1,m_2}^{xyy-+} &= \frac{32\dot\gamma_{|n-(m_1+m_2)|}}{L^3F_n^xF_{m_1}^yF_{m_2}^y}, & \xi_{n,m_1,m_2}^{xyy--} &= \frac{32\dot\gamma_{|n-|m_1-m_2||}}{L^3F_n^xF_{m_1}^yF_{m_2}^y},\end{aligned} \tag{9}$$

and we can calculate the four shear-pressure response coefficients by

$$\begin{aligned}\pi_{n,m_1,m_2}^{xyy++} &= \frac{32\Pi_{n+(m_1+m_2)}}{L^3F_n^xF_{m_1}^yF_{m_2}^y}, & \pi_{n,m_1,m_2}^{xyy+-} &= \frac{32\Pi_{|n+|m_1-m_2||}}{L^3F_1^xF_{m_1}^yF_{m_2}^y},\\ \pi_{n,m_1,m_2}^{xyy-+} &= \frac{32\Pi_{|n-(m_1+m_2)|}}{L^3F_n^xF_{m_1}^yF_{m_2}^y}, & \pi_{n,m_1,m_2}^{xyy--} &= \frac{32\Pi_{|n-|m_1-m_2||}}{L^3F_n^xF_{m_1}^yF_{m_2}^y}.\end{aligned} \tag{10}$$

In Sec. IV, we will evaluate these response functions over a range of SLF wavelengths. In this paper, we will only consider the case of $n = 1$ for the STF wave number. In Sec. V, we will use the response functions to predict some simple flow profiles. We will also show how they can be used to predict flow profiles for fluids under the influence of a single-component STF and a three-component SLF. First, we will briefly describe the computer simulation method used throughout this paper.

III. SIMULATION DETAILS

The simulation methods in this paper are the same as those used in [17]. We will only repeat the necessary information. The only difference between the system studied in this paper and the system used in [17] is that here we use multiple Fourier component SLFs. The equations of motion are therefore given by

$$\begin{aligned}\dot{\mathbf{r}}_i &= \frac{\mathbf{p}_i}{m},\\ \dot{\mathbf{p}}_i &= \mathbf{F}_i^\Phi + F_n^x\sin(k_ny_i)\mathbf{i} + \sum_q F_{m_q}^y\sin(k_{m_q}y_i)\mathbf{j}\\ &\quad - \alpha_0[\mathbf{p}_i - mu_x(y_i)\mathbf{i}],\end{aligned} \tag{11}$$

where $i = 1,2,\ldots,N$ labels the ith atom for a system of N atoms. $\mathbf{F}^\Phi$ is the force due to the interatomic potential. We use the Weeks, Chandler, and Andersen (WCA) potential given by

$$\phi_{\mathrm{WCA}}(r) = \begin{cases}4\epsilon\left[\left(\frac{\sigma}{r}\right)^{12} - \left(\frac{\sigma}{r}\right)^6\right] + \epsilon, & r \leqslant 2^{1/6}\sigma,\\ 0, & r > 2^{1/6}\sigma,\end{cases} \tag{12}$$

where σ and ϵ are the usual Lennard-Jones parameters. The WCA potential reproduces the generic structural properties of dense fluids, which are mainly determined by their hard-core interactions [18]. α_0 is the Nosé-Hoover integral feedback multiplier [19–21] calculated by solving $\dot\alpha_0 = (T - T_0)/\zeta$, where T is the instantaneous zero-wave-vector kinetic temperature, T_0 is the target value of the temperature, and ζ is the feedback strength constant. $m_1, m_2, \ldots$ label the set of SLF components with wave numbers $k_{m_1}, k_{m_2}, \ldots$. In this paper, we will consider systems with two- and three-component SLFs.

For all simulations, we use $N = 1372$ atoms. All quantities are given in standard Lennard-Jones reduced units, scaled by the atomic mass and the Lennard-Jones distance and energy parameters. The average reduced temperature is $T = 0.765$ and the average reduced density is $\rho = 0.685$, corresponding to a typical dense fluid state. All atoms have a reduced mass of $m_i = 1.0$, and the simulation cell lengths are $L_x = L_y = L_z = 12.605$ in reduced length units. With $n = 1$ for the STF and a suitable choice of the SLF wavelengths, we can generate flows in which one half-wavelength of the STF resembles a Poiseuille flow profile for a channel of width $L/2 = 6.3025$, i.e., approximately six molecular diameters. For water, this corresponds to a channel width of around 2 nm. The wavelengths of the SLFs are chosen so as to generate a range of density profiles including some closely resembling those found in planar channels. We obtain modulated density oscillations of wavelength $L/(2m)$, where $m = 6 \ldots 14$. At $m = 10$, the wavelength of the density oscillations is close to one molecular diameter, giving density profiles similar to those observed in simulations of dense fluids near hard walls.

To calculate the Fourier coefficients for the density profile, we use the direct Fourier decomposition method for the

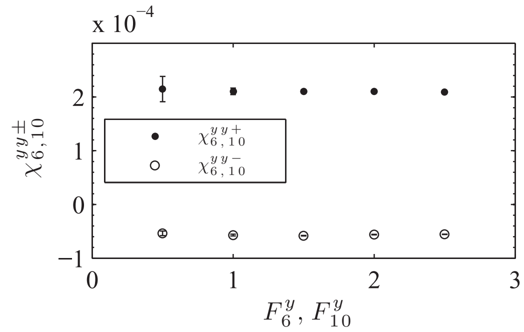

FIG. 1. Two examples of the SLF field strength dependence of the bilinear density response Fourier coefficients. Both SLF components have equal amplitude such that $F^y_{m_1} = F^y_{m_2} = 0.5$, 1.0, 1.5, 2.0, and 2.5.

instantaneous atomic configurations as described in [15,17,22]. The Fourier coefficients for the velocity and temperature profiles are determined by the least-squares method described by Baranyai [23] and others [16,17,24,25]. The Fourier coefficients of the shear-pressure profile are calculated directly from the expression for the wave-vector-dependent pressure tensor [17,22].

All results were obtained by averaging over 10 macroscopically equivalent but independent systems that were run for 2×10^6 time steps after reaching a stable steady state, as described in our previous paper [17].

IV. RESULTS FOR A SINGLE-COMPONENT STF AND TWO-COMPONENT SLFs

In Eq. (5) we showed that for each pair of distinct SLF components, we excite two harmonics in the density profile due to second-order bilinear coupling. In Eqs. (7) and (8) we showed that for each single-component STF and each pair of distinct SLF components, we excite four harmonics in the strain-rate and shear-pressure profiles due to third-order trilinear coupling. All of the other response components presented in these three equations were discussed in [17]. In this section, we evaluate the Fourier coefficients for the additional response functions that arise due to the addition of a second SLF component. Since the response functions should be evaluated in the limit of zero field strength, we will examine how the response function Fourier coefficients behave as the STF and SLF fields strengths are varied. We will see that none of the new response functions considered in this paper appear to have any systematic dependence of either the STF or SLF field strength over the range of fields investigated.

A. Bilinear density response functions

We begin with the bilinear density response coefficients $\chi^{yy+}_{m_1,m_2}$ and $\chi^{yy-}_{m_1,m_2}$ given by Eq. (6). As an example, in Fig. 1 we show how $\chi^{yy+}_{6,10}$ and $\chi^{yy-}_{6,10}$ behave over a range of SLF force amplitudes. We evaluate these coefficients from

$$\chi^{yy-}_{6,10} = \frac{8\rho_4}{L^2 F^y_6 F^y_{10}}, \quad \chi^{yy+}_{6,10} = \frac{8\rho_{16}}{L^2 F^y_6 F^y_{10}}. \tag{13}$$

Figure 1 shows results for Eq. (13) evaluated for $F^y_6 = F^y_{10} = 0.5$, 1.0, 1.5, 2.0, and 2.5. We see that both $\chi^{yy+}_{6,10}$ and $\chi^{yy-}_{6,10}$ are independent of the SLF field strength. We have confirmed that this independence holds for all possible combinations of pairs from $m = 6$, 8, 10, 12, and 14. Since the data points for $F^y_{m_1} = F^y_{m_2} = 0.5$ often have larger uncertainties, we exclude these values from our analysis. To evaluate the response function Fourier coefficients at zero field strength, it is therefore sufficient to calculate the average of the coefficients over the four field strengths from 1.0 to 2.5. We show numerical results for these calculations in Table I for all pair combinations of $m = 6$, 8, 10, 12, and 14.

TABLE I. Fourier coefficients of bilinear density response functions. The numbers in parentheses following the values are their uncertainties.

m_1,m_2	$\chi^{yy+}_{m_1,m_2}$ $(\times 10^{-4})$	$\chi^{yy-}_{m_1,m_2}$ $(\times 10^{-5})$
6,8	0.86 (0.12)	−4.1 (0.2)
6,10	2.1 (0.1)	−5.7 (0.2)
6,12	3.9 (0.2)	−3.4 (0.6)
6,14	2.0 (0.0)	4.9 (0.3)
8,10	2.3 (0.0)	−5.0 (0.1)
8,12	4.9 (0.1)	−4.0 (0.5)
8,14	2.9 (0.1)	3.6 (0.4)
10,12	7.1 (0.3)	−2.4 (0.8)
10,14	6.4 (0.3)	5.5 (0.2)
12,14	15.0 (1.9)	11.0 (1.0)

Because the bilinear density response function Fourier coefficients do not systematically depend on the SLF field strength, we can use a less computationally expensive method to evaluate them. Instead of performing the calculations over a range of SLF field strengths and then calculating an average value, we can just choose a single value for the field strength. In this way, we directly calculate $\chi^{yy+}_{m_1,m_2}$ and $\chi^{yy-}_{m_1,m_2}$ from Eq. (13). In this instance, we take $F^y_{m_1} = F^y_{m_2} = 2.0$. The response function Fourier coefficients $\chi^{yy+}_{m_1,m_2}$ and $\chi^{yy-}_{m_1,m_2}$ are two-dimensional functions in k space since they depend on the wavelengths of both SLF components. It is possible to evaluate these functions in specific domains of k space by evaluating Eq. (13) over a range of m_1 and m_2 values. In Fig. 2, we show five one-dimensional slices of $\chi^{yy+}_{m_1,m_2}$ and $\chi^{yy-}_{m_1,m_2}$. In particular, we show $\chi^{yy\pm}_{6,m_2}$, $\chi^{yy\pm}_{8,m_2}$, $\chi^{yy\pm}_{10,m_2}$, $\chi^{yy\pm}_{12,m_2}$, and $\chi^{yy\pm}_{14,m_2}$, evaluated over a range of m_2 such that $m_2 = 1,2,\ldots,20$.

It should be noted that we need to make various corrections when evaluating $\chi^{yy-}_{m_1,m_2}$. For example, when $m_1 = 6$ and $m_2 = 12$, the density Fourier component $\rho_6 \cos(k_6 y)$ consists of both a linear-response contribution from F^y_6 and a bilinear-response contribution since $|m_1 - m_2| = 6$. We correct $\chi^{yy-}_{6,12}$ by letting $\chi^{yy-}_{6,12} = 8(\rho_6 + LF^y_6\chi^y_6)/L^2F^y_6F^y_{12}$. χ^y_6 is taken from Ref. [17]. As a second example, consider the case in which $m_1 = 6$ and $m_2 = 2$. In this case, the density Fourier component $\rho_4 \cos(k_4 y)$ again has two contributions: a second-order response contribution from F^y_2 and a bilinear-response contribution since $|m_1 - m_2| = 4$. To correct for the additional contributions, we calculate $\chi^{yy-}_{6,2}$ from $\chi^{yy-}_{6,2} = 8(\rho_4 - L^2F^y_2F^y_2\chi^{yy}_{2,2}/8)/L^2F^y_6F^y_2$.

B. Trilinear strain-rate and shear-pressure response

We now evaluate the Fourier coefficients for the trilinear response functions given by Eqs. (9) and (10). For all

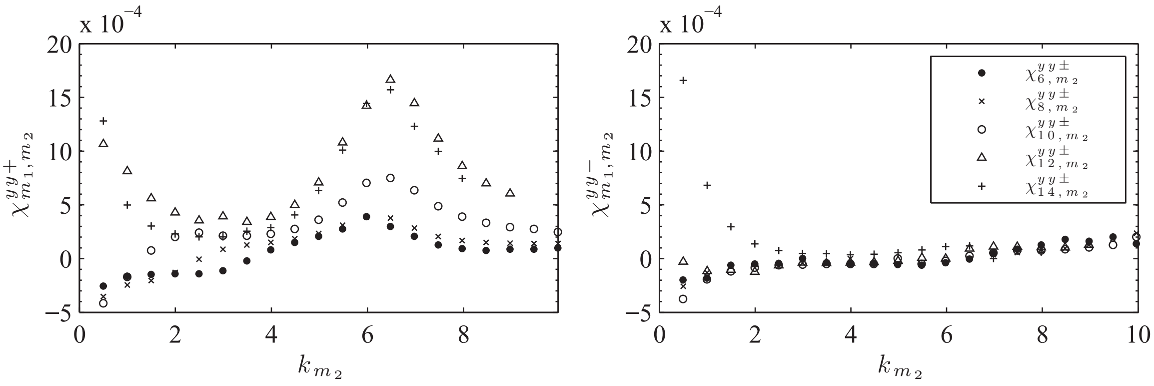

FIG. 2. Fourier space bilinear response function shown for one-dimensional slices through the full two-dimensional space.

systems in this paper, we take $n = 1$ and so the STF is $F^x(y) = F_1^x \sin(k_1 y)$. Therefore, the Fourier coefficients of the corresponding strain-rate and shear-pressure response functions are $\xi^{xyy\pm\pm}_{1,m_1,m_2}$ and $\pi^{xyy\pm\pm}_{1,m_1,m_2}$. We wish to determine whether these Fourier coefficients of the response functions depend on the force amplitudes. As an example, in Fig. 3 we show $\xi^{xyy++}_{1,6,10}$ and $\pi^{xyy++}_{1,6,10}$ calculated over a range of SLF force amplitudes for a single STF force amplitude $F_1^x = 0.10$. From Eq. (7), we have

$$\xi^{xyy++}_{1,6,10} = \frac{32 k_{17} u_{17}}{L^3 F_1^x F_6^y F_{10}^y}, \quad \pi^{xyy++}_{1,6,10} = \frac{32 \Pi_{17}}{L^3 F_1^x F_6^y F_{10}^y}. \tag{14}$$

For the two-component SLF, we use equal force amplitudes such that $F_6^y = F_{10}^y = 1.0$, 1.5, 2.0, 2.5, 3.0, 3.5, and 4.0. We neglect the data points for the lower SLF amplitudes $F_6^y = F_{10}^y = 1.0$, 1.5, and 2.0 since the data have large uncertainties for these values. In the region of $F_6^y = F_{10}^y = 2.5$, 3.0, 3.5, and 4.0, the coefficients are essentially independent of the SLF amplitude. We calculate the averages of $\xi^{xyy++}_{1,6,10}$ and $\pi^{xyy++}_{1,6,10}$ in this region. We plot these averages as a function of STF field strength to check the STF amplitude dependence. This is done in Fig. 4 for all $\xi^{xyy\pm\pm}_{1,6,10}$ and $\pi^{xyy\pm\pm}_{1,6,10}$ coefficients.

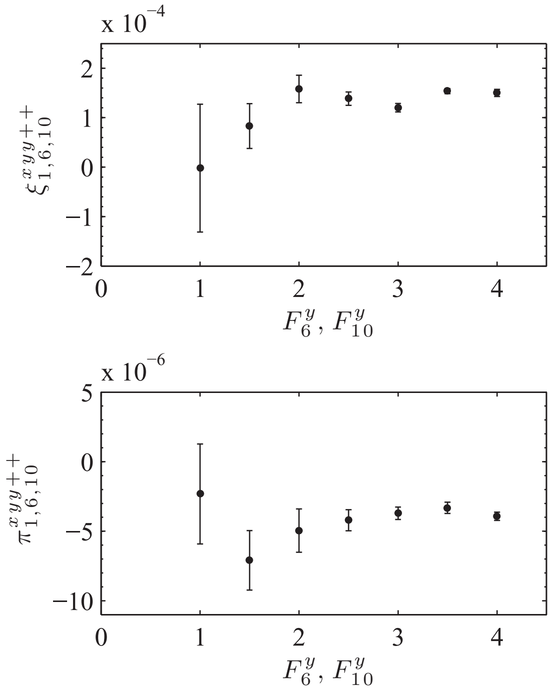

FIG. 3. Examples of the SLF dependence of the trilinear strain-rate and shear-pressure response function Fourier coefficients for $n = 1$, $m_1 = 6$, and $m_2 = 10$. Single STF field strength used $F_1^x = 0.10$.

Note that in the case of $\xi^{xyy+-}_{1,6,10}$ and $\pi^{xyy+-}_{1,6,10}$, we need to calculate a correction due to bilinear contributions at the same wave number. For the strain-rate response, we calculate $\xi^{xyy+-}_{1,6,10} = 32(k_5 u_5 - \frac{L^2}{8} F_1^x F_6^y \xi^{xy-}_{1,6})/L^3 F_1^x F_6^y F_{10}^y$, and for the shear-pressure response we calculate $\pi^{xyy+-}_{1,6,10} = 32(\Pi_5 - \frac{L^2}{8} F_1^x F_6^y \xi^{xy-}_{1,6})/L^3 F_1^x F_6^y F_{10}^y$. $\xi^{xy-}_{1,6}$ and $\pi^{xy-}_{1,6}$ are taken from Ref. [17].

From Fig. 4 we see that all $\xi^{xyy\pm\pm}_{1,6,10}$ and $\pi^{xyy\pm\pm}_{1,6,10}$ coefficients appear to be independent of the STF amplitude. We therefore calculate the average of these values. In this way, we are calculating two averages to evaluate the ultimate value of a response coefficient: the average over the range of SLF amplitudes for each value of the STF, and then the average of these averages over the range of STF amplitudes. Alternatively, we can reduce the number of simulations used to evaluate the coefficients. Instead of calculating $\xi^{xyy\pm\pm}_{1,m_1,m_2}$ and $\pi^{xyy\pm\pm}_{1,m_1,m_2}$ over a range of SLF amplitudes, we use a single-amplitude $F_{m_1}^y = F_{m_2}^y = 3.0$, which we see from Fig. 3 is in the region where we can be confident that the trilinear coefficients are similar to the average value of the coefficient. With the same range of STF amplitudes as above, $F_1^x = 0.05$, 0.10, 0.15, and 0.20, we calculate $\xi^{xyy\pm\pm}_{1,m_1,m_2}$ and $\pi^{xyy\pm\pm}_{1,m_1,m_2}$ for the single SLF amplitude and then calculate the average over the range of STF amplitudes. In Table II, we show $\xi^{xyy\pm\pm}_{1,m_1,m_2}$ and $\pi^{xyy\pm\pm}_{1,m_1,m_2}$ calculated in this way for various pairs of m_1 and m_2.

We must be careful when calculating the values in Table II to account for many cases in which there are multiple response contributions to a particular Fourier component of the strain rate and shear pressure. For example, when $|m_1 - m_2| = 2$, then ξ^{xyy--}_{n,m_1,m_2} and π^{xyy--}_{n,m_1,m_2} both represent coefficients for harmonics with wave number $k_1 = 2\pi/L_y$. In this case, we need to subtract the linear response (and, in the case of the strain rate, the third-order response due to ξ^{xyy0}_{n,m_1,m_1} and ξ^{xyy0}_{n,m_2,m_2}) from the strain rate and shear pressure, in order to calculate ξ^{xyy--}_{n,m_1,m_2} and π^{xyy--}_{n,m_1,m_2} correctly.

Finally, it is interesting to note the small magnitudes of all $\pi^{xyy\pm\pm}_{1,m_1,m_2}$ terms. In many cases, the uncertainty in the coefficient

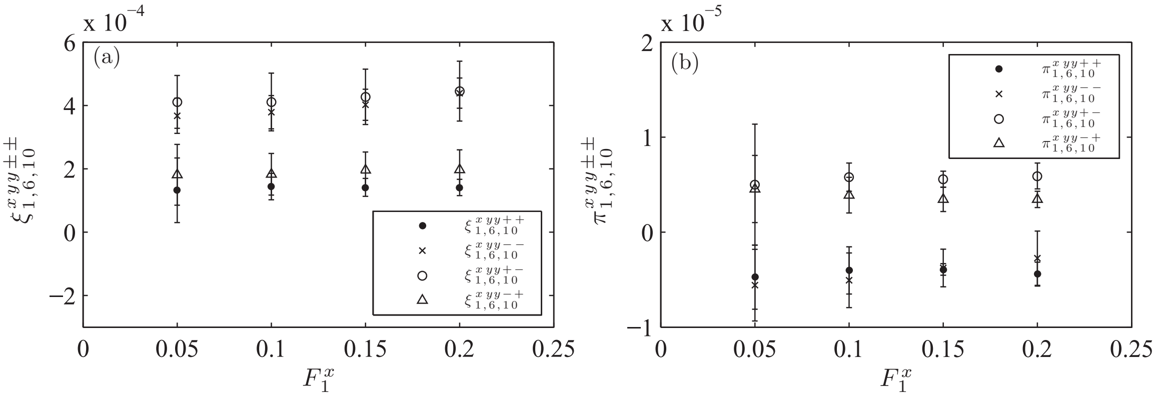

FIG. 4. STF dependence of the four $\xi^{xyy\pm\pm}_{1,6,10}$ coefficients and the four $\pi^{xyy\pm\pm}_{1,6,10}$ coefficients.

is approximately equal to, or perhaps even larger than, the value of the coefficient. For example, we see that $\pi^{xyy+-}_{1,6,12} = 0.2 \pm 1.8$. Therefore, the trilinear contributions to the shear pressure are often negligible at the currently achievable limits of precision.

V. PREDICTING DENSITY, VELOCITY, AND SHEAR-PRESSURE PROFILES FOR A SINGLE-COMPONENT STF AND TWO-COMPONENT SLFs

In this section, we use the Fourier coefficients for the response functions calculated in Sec. IV and in our previous paper [17] in the truncated functional expansions to predict various density, velocity, and shear-pressure profiles produced with a single-component STF and two component SLFs. We will compare the results with profiles obtained directly from MD simulations.

A. Density profiles

For the force given by Eq. (3) with $n = 1$, we expect a density profile given by

$$\begin{aligned}\rho(y) = \rho_0 &- \frac{L}{2}F^y_{m_1}\chi^y_{m_1}\cos(k_{m_1}y) - \frac{L}{2}F^y_{m_2}\chi^y_{m_2}\cos(k_{m_2}y)\\ &+ \frac{L^2}{8}F^y_{m_1}F^y_{m_1}\chi^{yy}_{m_1,m_1}\cos(k_{2m_1}y) + \frac{L^2}{8}F^y_{m_2}F^y_{m_2}\chi^{yy}_{m_2,m_2}\\ &\times\cos(k_{2m_2}y) + \frac{L^2}{8}F^y_{m_1}F^y_{m_2}\chi^{yy-}_{m_1,m_2}\cos(k_{|m_1-m_2|}y)\\ &+ \frac{L^2}{8}F^y_{m_1}F^y_{m_2}\chi^{yy+}_{m_1,m_2}\cos(k_{m_1+m_2}y)\\ &+ \frac{L^2}{8}F^x_1F^x_1\chi^{xx}_{1,1}\cos(k_2y),\end{aligned} \tag{15}$$

TABLE II. Third-order trilinear strain-rate and shear-pressure response function Fourier coefficients for various pairs of two-component SLFs. All evaluated with a single-component STF at $n = 1$. The numbers in parentheses following the values are their uncertainties.

m_1,m_2	ξ^{xyy++}_{1,m_1,m_2} ($\times 10^{-4}$)	ξ^{xyy+-}_{1,m_1,m_2} ($\times 10^{-4}$)	ξ^{xyy-+}_{1,m_1,m_2} ($\times 10^{-4}$)	ξ^{xyy--}_{1,m_1,m_2} ($\times 10^{-4}$)
6,8	0.91 (0.27)	2.5 (0.3)	1.1 (0.3)	2.7 (0.4)
6,10	1.3 (0.3)	4.2 (0.2)	1.9 (0.3)	3.8 (0.5)
6,12	3.0 (0.5)	7.4 (0.6)	3.3 (06)	8.0 (0.6)
6,14	1.3 (0.6)	0.62 (0.17)	1.5 (0.5)	1.4 (0.3)
8,10	1.5 (0.3)	4.0 (0.4)	1.6 (0.3)	5.0 (0.7)
8,12	2.9 (0.6)	6.0 (0.6)	2.9 (0.2)	6.9 (0.8)
8,14	1.4 (0.4)	1.4 (0.3)	1.2 (0.7)	1.5 (0.2)
10,12	4.5 (0.8)	8.4 (1.1)	5.2 (0.7)	12 (2)
10,14	1.4 (0.7)	2.2 (0.3)	1.5 (0.7)	2.7 (0.4)
12,14	1.4 (0.5)	1.3 (0.6)	0.87 (0.90)	0.59 (1.0)
m_1,m_2	π^{xyy++}_{1,m_1,m_2} ($\times 10^{-6}$)	π^{xyy+-}_{1,m_1,m_2} ($\times 10^{-6}$)	π^{xyy-+}_{1,m_1,m_2} ($\times 10^{-6}$)	π^{xyy--}_{1,m_1,m_2} ($\times 10^{-5}$)
6,8	−1.8 (1.3)	5.4 (3.4)	2.1 (1.4)	−1.6 (0.6)
6,10	−3.3 (2.6)	5.8 (1.0)	4.2 (2.2)	−0.42 (0.23)
6,12	−7.1 (0.6)	0.2 (1.8)	8.0 (0.9)	0.07 (0.16)
6,14	−3.0 (1.2)	−1.4 (1.5)	3.2 (0.9)	0.0 (0.1)
8,10	−4.1 (1.0)	6.6 (3.2)	3.9 (1.5)	−2.0 (0.6)
8,12	−5.2 (0.9)	1.6 (1.8)	6.0 (0.9)	−0.20 (0.3)
8,14	−3.6 (2.1)	2.2 (1.5)	3.7 (0.9)	0.17 (0.19)
10,12	−9.5 (1.2)	4.5 (4.3)	10 (1)	−1.2 (1.0)
10,14	−7.6 (1.2)	−2.3 (2.1)	8.0 (1.3)	0.66 (0.19)
12,14	−16 (1)	−9.2 (2.6)	17 (2)	0.27 (0.79)

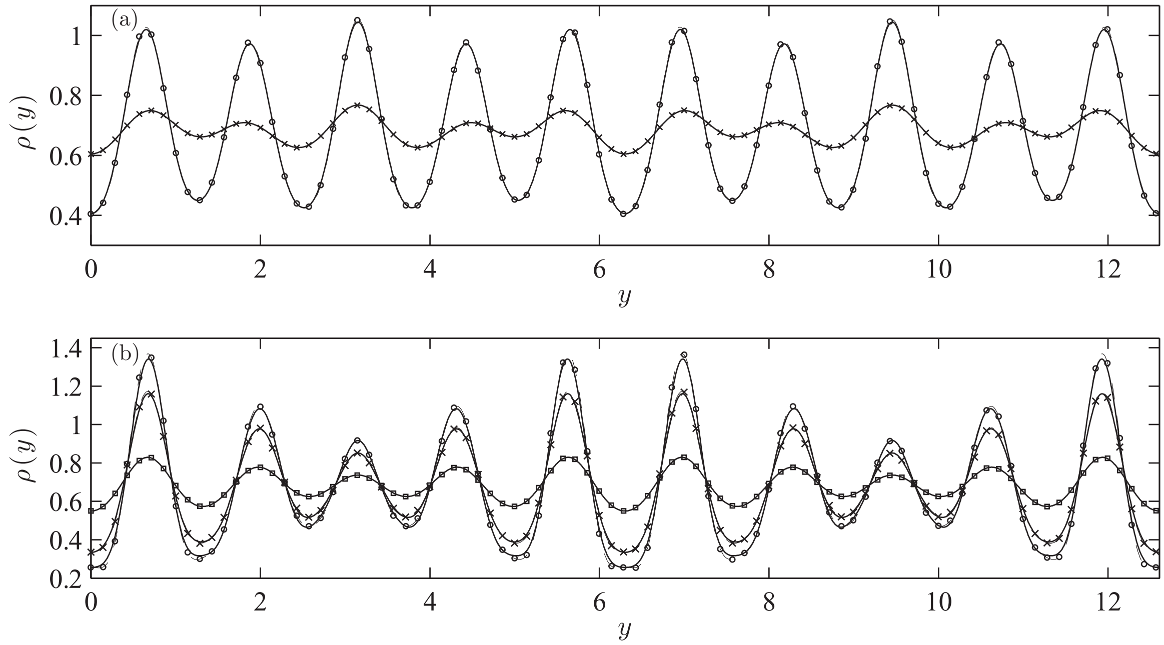

FIG. 5. Comparison between density profiles obtained directly from MD simulations and those predicted by truncated functional expansions with independently computed response functions, for a single-component STF combined with two-component SLFs. Bold lines without symbols represent MD simulations. STF has $F_1^x = 0.08$ for all profiles. (a) $m_1 = 6$ and $m_2 = 10$. Thin dashed lines indicated with crosses represent $F_6^y = 1.0, F_{10}^y = 0.5$, and thin dashed lines indicated with circles represent $F_6^y = 1.0, F_{10}^y = 3.0$. (b) $m_1 = 8$ and $m_2 = 10$. Thin dashed lines indicated with squares represent $F_8^y = F_{10}^y = 1.0$, crosses represent $F_8^y = F_{10}^y = 3.0$, and circles represent $F_8^y = F_{10}^y = 4.0$.

where we have truncated the functional expansion at the second-order response. This expression can be obtained substituting Eq. (5) into the density Fourier series in Eq. (4). We can reconstruct the density profiles produced by a single-component STF and two-component SLFs using the values of the bilinear response functions given in Table I and the values for the first- and second-order single-component SLF response functions given in [17]. In Fig. 5, we show two sets of example density profiles. Figure 5(a) shows data for $m_1 = 6$ and $m_2 = 10$. Figure 5(b) shows data for $m_1 = 8$ and $m_2 = 10$. The force amplitudes are given in the figure caption. The bold lines show the MD simulation results, and the thin lines indicated with symbols show the predictions of the truncated functional expansion using the previously calculated response functions. The symbols do not indicate discrete data points since all of the profiles are functions constructed by Fourier synthesis. We use the symbols only to distinguish the different profiles. The MD simulation results and the predictions are in very good agreement, so it is difficult to distinguish the compared profiles. The relative difference is of the order of 1% for $F = 0.5$ and 5% for $F = 3.0$ at most. To calculate the relative difference, we normalized the residuals using the zero-wave-vector density component. In Fig. 5(b), we can see at the density minima of the profile for $F_8^y = F_{10}^y = 4.0$ that there is a small but observable difference between the prediction and the MD profile. At these regions, the difference is approximately 5%. The force amplitudes are relatively large, so it is likely that the difference is due to third-order effects, as we described in [15]. Figure 6 shows a magnified view to emphasize the contribution of each order of response to the total density profile. We show the convergence of the prediction given by Eq. (15) toward the MD simulation profiles as we add additional orders of response. We show this convergence for the case of $m_1 = 8$, $m_2 = 10$, and $F_8^y = F_{10}^y = 4.0$, which is the density profile with the largest amplitude in Fig. 5(c). The region near the first peak is magnified in Fig. 6. The bold line represents the density profile calculated directly from the MD simulations. The thin dashed lines indicated with symbols represent the different orders of truncation. We see that the linear response alone (crosses) is insufficient to describe the density profiles, as expected. The circles show second-order predictions without the inclusion of the bilinear response terms

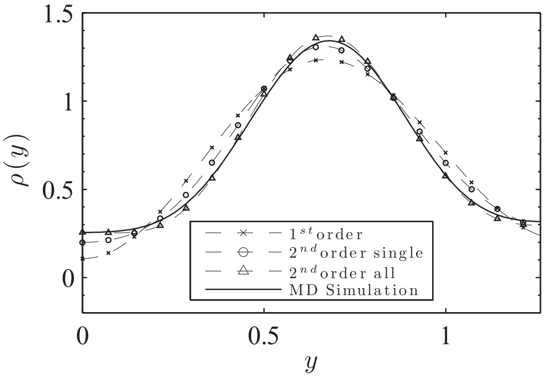

FIG. 6. Convergence of the truncated expansion density profile toward the MD density profile. Magnification of the first peak in Fig. 5(b) for $F_8^y = F_{10}^y = 4.0$. The thick line represents the MD density. Thin dashed lines indicated with symbols represent different orders of truncation.

described in the previous section. When we include the bilinear terms (triangles), we greatly improve the prediction. We see that there are still differences between the prediction and the MD simulation profile, but they are quite small. Again, it is most likely that we could further improve the predictions by including the third-order response in our treatment. We conclude that a truncated functional expansion including the first- and second-order response terms is sufficient to predict the total density response under these conditions.

B. Velocity profiles

For the force given by Eq. (3) with $n = 1$, we expect a velocity profile given by

$$
\begin{aligned}
u(y) ={}& -\frac{L}{2} F_1^x \frac{\xi_1^x}{k_1} \sin(k_1 y) + \frac{L^2}{8} F_1^x F_{m_1}^y \left[\frac{\xi_{1,m_1}^{xy-}}{k_{|1-m_1|}} \sin(k_{|1-m_1|} y) + \frac{\xi_{1,m_1}^{xy+}}{k_{1+m_1}} \sin(k_{1+m_1} y) \right] + \frac{L^2}{8} F_1^x F_{m_2}^y \left[\frac{\xi_{1,m_2}^{xy-}}{k_{|1-m_2|}} \sin(k_{|1-m_2|} y) \right. \\
&\left. + \frac{\xi_{1,m_2}^{xy+}}{k_{1+m_2}} \sin(k_{1+m_2} y) \right] + \frac{L^3}{32} F_1^x F_{m_1}^y F_{m_1}^y \left[\frac{\xi_{1,m_1,m_1}^{xyy-}}{k_{|1-2m_1|}} \sin(k_{|1-2m_1|} y) + \frac{\xi_{1,m_1,m_1}^{xyy0}}{k_1} \sin(k_1 y) + \frac{\xi_{1,m_1,m_1}^{xyy+}}{k_{1+2m_1}} \sin(k_{1+2m_1} y) \right] \\
&+ \frac{L^3}{32} F_1^x F_{m_2}^y F_{m_2}^y \left[\frac{\xi_{1,m_2,m_2}^{xyy-}}{k_{|1-2m_2|}} \sin(k_{|1-2m_2|} y) + \frac{\xi_{1,m_2,m_2}^{xyy0}}{k_1} \sin(k_1 y) + \frac{\xi_{1,m_2,m_2}^{xyy+}}{k_{1+2m_2}} \sin(k_{1+2m_2} y) \right] \\
&+ \frac{L^3}{32} F_1^x F_{m_1}^y F_{m_2}^y \left[\frac{\xi_{1,m_1,m_2}^{xyy++}}{k_{1+(m_1+m_2)}} \sin(k_{1+(m_1+m_2)} y) + \frac{\xi_{1,m_1,m_2}^{xyy+-}}{k_{|1+|m_1-m_2||}} \sin(k_{|1+|m_1-m_2||} y) \right. \\
&\left. + \frac{\xi_{1,m_1,m_2}^{xyy-+}}{k_{|1-(m_1+m_2)|}} \sin(k_{|1-(m_1+m_2)|} y) + \frac{\xi_{1,m_1,m_2}^{xyy--}}{k_{|1-|m_1-m_2||}} \sin(k_{|1-|m_1-m_2||} y) \right]. \qquad (16)
\end{aligned}
$$

This equation for the velocity can be determined using the equation for the Fourier space representation of the strain rate Eq. (7). The velocity profile is shown because it is easier to visualize than the strain-rate profile.

In the second and third lines of Eq. (16), we see the bilinear couplings between the single-component STF and each single-component SLF. In the next two lines, we see the third-order coupling between the single-component STF and quadratic contributions from each single-component SLF. These terms were discussed in [17]. In addition, we see the inclusion of the four trilinear terms that were described in Sec. IV. The values for the linear-response functions given in Ref. [17] and in Table II can now be used to construct the velocity profiles.

In Fig. 7, we show some examples of velocity profiles produced using the force given by Eq. (3). We only show the velocity profile over half of the simulation box length. The systems are the same as those introduced in the previous section, i.e., for the same set of forces used to produce the density profiles in Fig. 5. The relative residuals are also shown. The residuals are scaled using the amplitudes of the MD simulation profiles. In Fig. 7(a), where $m_1 = 6$ and $m_2 = 10$, we see that the predictions of the truncated functional expansion with independently computed response functions are accurate. The relative difference is between 1% and 5% at most. In Fig. 7(b), where $m_1 = 8$ and $m_2 = 10$, we can see that for the larger SLF amplitudes, there is a small difference between the MD simulations and the truncated functional expansion predictions. The difference between the two profiles is observable when $F_8^y = F_{10}^y = 3.0$, but it greatly increases when we increase the SLF amplitudes to $F_8^y = F_{10}^y = 4.0$. It should be kept in mind that these are very large force amplitudes.

In Fig. 8 we consider the convergence of the velocity profile given by the truncated functional expansion to the velocity profile calculated directly from the MD simulation for the case in which $m_1 = 8$ and $m_2 = 10$, $F_1^x = 0.08$, and $F_8^y = F_{10}^y = 3.0$, which is the second largest profile in Fig. 7(c). We show the convergence in two different ways. The first, in Fig. 8(a), shows how the series in Eq. (16) approaches

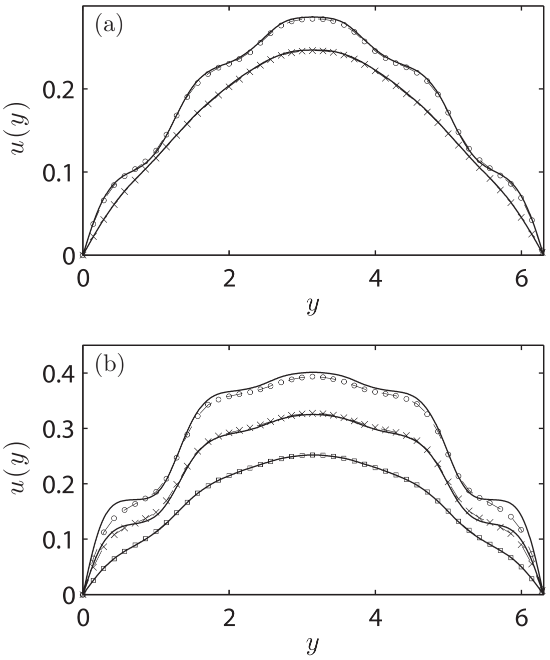

FIG. 7. Comparison between velocity profiles obtained directly from MD simulation with predictions of the truncated functional expansion for a single-component STF and two-component SLFs. Bold lines represent MD simulations, thin dashed lines with symbols represent predictions. The system parameters are the same as those used in Fig. 5. Velocity profiles are only shown for half of a wave cycle.

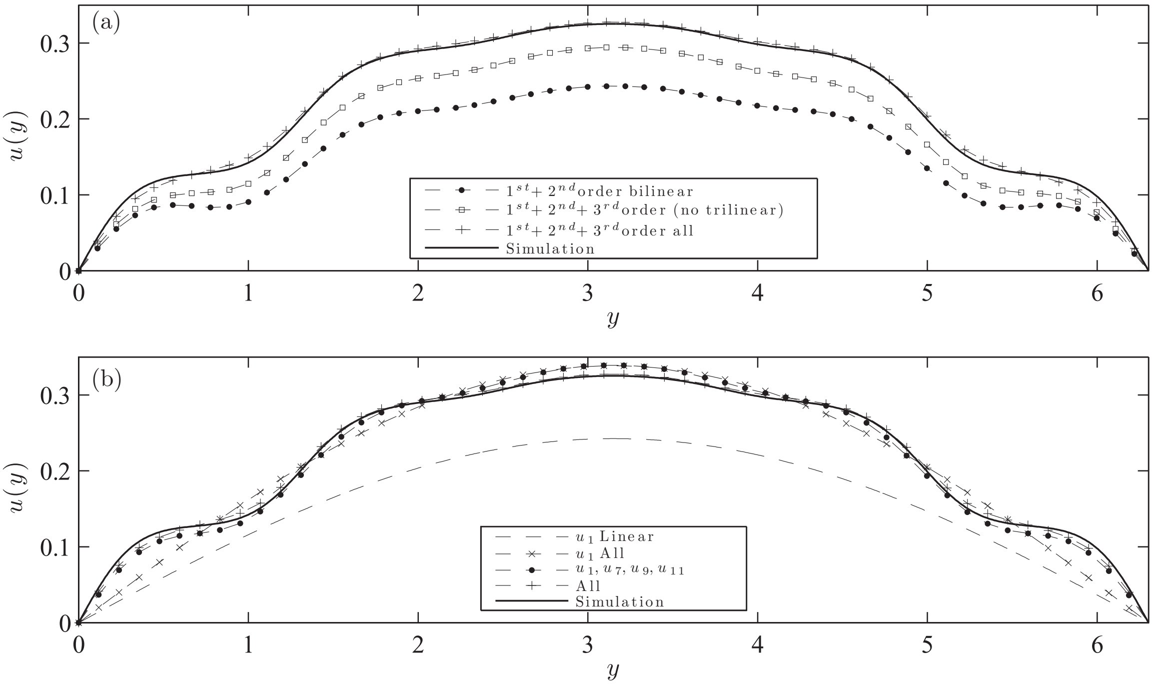

FIG. 8. Convergence of the Fourier series velocity profile Eq. (16) toward the MD simulation profile for $m_1 = 8$, $m_2 = 10$, $F_1^x = 0.08$, and $F_8^y = F_{10}^y = 3.0$. (a) Convergence for increasing orders of response. (b) Convergence for the addition of increasingly shorter wavelengths. Velocity profiles are only shown for half of a wave cycle.

the MD simulation profile as we add increasing orders of response. For the third-order contributions, we distinguish between a series that includes only the third-order terms that are due to the single-component STF and single SLF, as described in Ref. [17], and a series that includes the third-order trilinear terms. The former is labeled as "no trilinear" in the figure legend. This plot is interesting for two reasons. First, it shows that the short-wavelength oscillations in the velocity profile are largely due to the second-order bilinear terms. Second, it shows the significant contribution to the total velocity profile at the fundamental wave number made by the third-order terms. There are three third-order response contributions to the fundamental velocity component: one given by $\xi_{1,8,8}^{xyy0}$, one by $\xi_{1,10,10}^{xyy0}$, and one due to the third-order trilinear response $\xi_{1,8,10}^{xyy--}$.

In Fig. 8(b), we show how the series in Eq. (16) approaches the MD simulation profile as we add terms with progressively shorter wavelengths. We show $u_1 \sin(k_1 y)$ for the linear response only, and also for the linear plus all third-order contributions. $u_3 \sin(k_3 y)$ only makes a small contribution, so we only include it when we include all terms. Next we add $u_7 \sin(k_7 y)$, $u_9 \sin(k_9 y)$, and $u_{11} \sin(k_{11} y)$. These are the harmonics that are excited due to the bilinear response for $n = 1$, $m_1 = 8$ and for $n = 1$, $m_2 = 10$. Figure 8(b) confirms that the short-wavelength oscillations in the velocity profile are mostly due to the bilinear terms. Including shorter-wavelength terms in the series has little effect on the total profile. We are able to conclude that the inadequacy in the truncated functional expansion prediction of the velocity profile, which is clearest where the velocity oscillations are greatest, is due to additional contributions to the velocity at the $u_7 \sin(k_7 y)$, $u_9 \sin(k_9 y)$, and $u_{11} \sin(k_{11} y)$ components, which are not accounted for by the bilinear response alone. There are higher-order contributions to the velocity profile at these wavelengths that we have neglected, and it is likely that for larger SLF amplitudes, these terms provide a more significant contribution to the total velocity profile.

C. Shear-pressure profiles

For the force given by Eq. (3) with $n = 1$, we expect the shear-pressure profile to be given by

$$\begin{aligned}\Pi(y) = &-\frac{L}{2} F_1^x \pi_1^x \cos(k_1 y) + \frac{L^2}{8} F_1^x F_{m_1}^y \big[\pi_{1,m_1}^{xy-} \cos(k_{|1-m_1|} y) + \pi_{1,m_1}^{xy+} \cos(k_{1+m_1} y)\big] + \frac{L^2}{8} F_1^x F_{m_2}^y \big[\pi_{1,m_2}^{xy-} \cos(k_{|1-m_2|} y) \\ &+ \pi_{1,m_2}^{xy+} \cos(k_{1+m_2} y)\big] + \frac{L^3}{32} F_1^x F_{m_1}^y F_{m_1}^y \big[\pi_{1,m_1,m_1}^{xyy-} \cos(k_{|1-2m_1|} y) + \pi_{1,m_1,m_1}^{xyy+} \cos(k_{1+2m_1} y)\big] \\ &+ \frac{L^3}{32} F_1^x F_{m_2}^y F_{m_2}^y \big[\pi_{1,m_2,m_2}^{xyy-} \cos(k_{|1-2m_2|} y) + \pi_{1,m_2,m_2}^{xyy+} \cos(k_{1+2m_2} y)\big] + \frac{L^3}{32} F_1^x F_{m_1}^y F_{m_2}^y \big[\pi_{1,m_1,m_2}^{xyy++} \cos(k_{1+(m_1+m_2)} y) \\ &+ \pi_{1,m_1,m_2}^{xyy+-} \cos(k_{|1+|m_1-m_2||} y) + \pi_{1,m_1,m_2}^{xyy-+} \cos(k_{|1-(m_1+m_2)|} y) + \pi_{1,m_1,m_2}^{xyy--} \cos(k_{|1-|m_1-m_2||} y)\big]. \end{aligned} \quad (17)$$

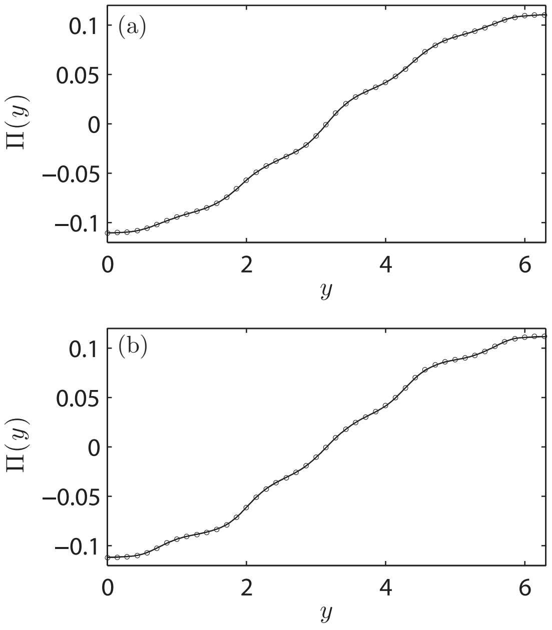

FIG. 9. Comparison between shear-pressure profiles obtained from MD simulation and predictions of the truncated functional expansion with independently computed response functions. Bold lines represent MD simulations, thin dashed lines with symbols represent predictions. Both plots are for $F_1^x = 0.08$. (a) $m_1 = 6$ and $m_2 = 10$ with $F_6^y = 1.0, F_{10}^y = 3.0$. (b) $m_1 = 8$ and $m_2 = 10$ with $F_8^y = F_{10}^y = 3.0$. Shear-pressure profiles only shown for half of a wave cycle.

Unlike the velocity profile, the shear-pressure profile does not include the π_{1,m_1,m_1}^{xyy0} and π_{1,m_2,m_2}^{xyy0} terms since we have previously shown that these terms are zero [17]. The $\pi_{1,m_1,m_2}^{xyy\pm\pm}$ coefficients are evaluated in Table II for $n = 1$ and various pair combinations of m_1 and m_2.

In Fig. 9 we show two examples of shear-pressure profiles. We only show the profiles over half of the simulation box length. Figure 9(a) shows a comparison between the truncated functional expansion prediction, given by Eq. (17) for $m_1 = 6$, $m_2 = 10$, $F_6^y = 1.0$, and $F_{10}^y = 3.0$, and the MD simulation results. Figure 9(b) shows the comparison for $m_1 = 8$, $m_2 = 10$, and $F_6^y = F_{10}^y = 3.0$. We can see that there is excellent agreement between the prediction and the MD simulation results.

The convergence plot in Fig. 10 shows the contribution of the different orders of response to the shear pressure. The plot shows only a small part of the full profile. We see that, unlike the velocity profile, the shear-pressure profile contains no apparent contribution at the fundamental wavelength due to the nonlinear response. Most of the oscillation in the shear stress is due to the bilinear response, but the third-order response slightly improves the accuracy of the prediction.

VI. PREDICTING DENSITY, VELOCITY, AND SHEAR-PRESSURE PROFILES FOR A SINGLE-COMPONENT STF AND A THREE-COMPONENT SLF

In this final section, we investigate whether the density, velocity, and shear-pressure profiles for a fluid under the influence of a single-component STF and a three-component SLF can be described using functional expansions truncated at second order for the density response and third order for the strain-rate and shear-pressure responses. Note that, due to symmetry, there can be no contribution to the first- or second-order density response from terms that couple all three SLF components. Also there can be no first-, second-, or third-order contributions to the velocity or shear pressure from terms that couple the single STF component and all three SLF components. It is our intention to test whether it is necessary to include additional terms to account for the four force component couplings or whether the density, velocity and shear-pressure profiles can be suitably predicted using orders of response that have already been discussed. If we can simplify the description, then the way is open to predicting density, velocity, and shear-pressure profiles for systems with many-component SLFs, such as those that might be used to model Fourier-synthesized channel-like density profiles, without the need to continually acquire additional response functions of increasing order every time we add another SLF component.

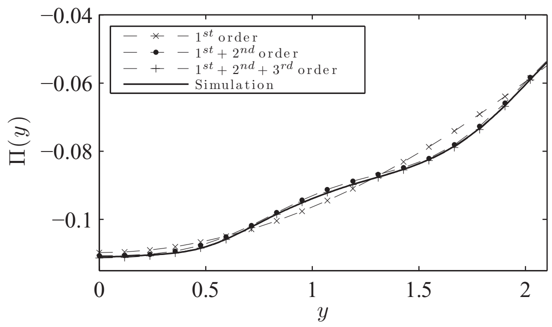

FIG. 10. Convergence of the shear-pressure profile predicted by Eq. (17) toward the MD simulation profile for $m_1 = 8$, $m_2 = 10$, $F_1^x = 0.08$, and $F_8^y = F_{10}^y = 3.0$. Shear-pressure profiles only shown for half of a wave cycle.

For this investigation, we will use the following specific composite force with a single-component STF and a three-component SLF:

$$\mathbf{F}(y) = \big(F_1^x \sin(k_1 y), F_6^y \sin(k_6 y) + F_8^y \sin(k_8 y) + F_{10}^y \sin(k_{10} y)\big). \tag{18}$$

We do not include the explicit Fourier expansions of the fluid profiles as we did for the two-component SLF system in Eqs. (15), (16), and (17). Since we do not introduce any additional orders of coupling, Eqs. (15), (16), and (17) can be used as a guide for constructing the profiles for a three-SLF system by simply combining the terms from the three two-SLF-component systems, being sure to leave out any repeat occurrences of terms.

A. Density profiles

In Fig. 11(a), we show a comparison between the MD simulation density profiles and the truncated functional expansion predictions for the density profiles produced by the force given in Eq. (18). In the functional expansion, there are three linear-response terms, one for each value of m, three quadratic

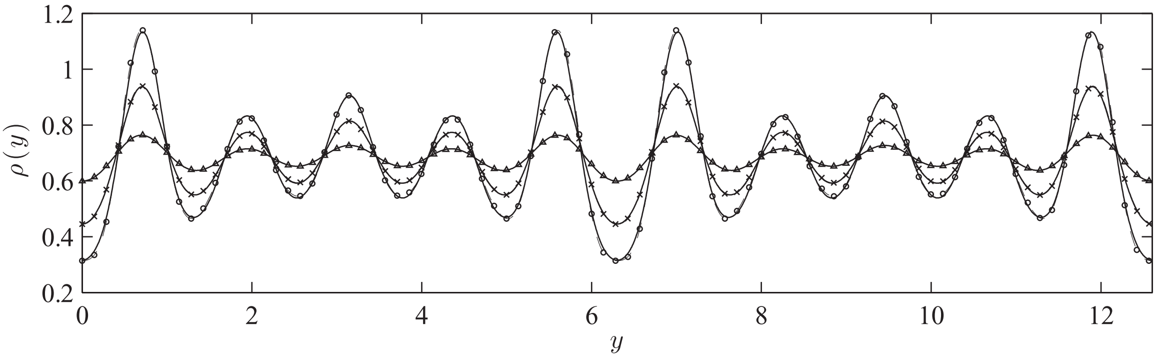

FIG. 11. Comparison between density profiles directly from MD simulations and the predictions of the truncated functional expansion using previously computed response functions for three-component SLFs. $m_1 = 6$, $m_2 = 8$, and $m_3 = 10$. Bold lines without symbols represent MD simulations. Thin dashed lines indicated with triangles are for $F_6^y = F_8^y = F_{10}^y = 0.5$. Thin dashed lines indicated with crosses are for $F_6^y = F_8^y = F_{10}^y = 1.5$. Thin dashed lines indicated with circles are for $F_6^y = F_8^y = F_{10}^y = 2.5$.

second-order response terms, again one for each value of m, six bilinear response terms for all pair couplings, and a single second-order shear-induced term due to the STF. We show three profiles produced such that $F_6^y = F_8^y = F_{10}^y = 0.5$, 1.5, and 2.5. For all profiles, the STF has an amplitude $F_1^x = 0.08$. We see that our prediction gives a good representation of the density profile from the MD simulation. The greatest deviation, which is clearest at the lowest density minima, occurs for the largest field strength. For the system with the largest field strengths, the greatest relative difference between the truncated expansion and the MD profiles is 4%. To calculate the relative difference, we normalized the residuals using the zero-wave-vector density component.

In Fig. 12, we show the convergence of the Fourier series density profile toward the MD simulation results. We show results for the density profile produced with the largest field strength $F_6^y = F_8^y = F_{10}^y = 2.5$. Figure 12 shows a magnification of the first peak of this profile. We see that including the three quadratic second-order response terms alone does not greatly improve the agreement. It is the bilinear second-order response that is crucial for accurate predictions. These are very large field strengths, so again it is likely that the small remaining discrepancies are due to a third-order response to each of the single-component SLFs. It is also possible that there is a contribution from terms corresponding to three-SLF-component coupling. It is clear that the truncated expansion gives good agreement with the MD simulation profile. We can say that the prediction of the density profile is quite good even without three-SLF-component coupling. This is a promising result when we consider the possibility of producing density profiles with many-component SLFs.

B. Velocity profiles

Figure 13 shows the velocity profiles produced using Eq. (18) for the same combinations of force amplitudes used to produce the density profiles in Fig. 11. We compare the MD simulations with predictions. The Fourier series expansion has a single linear-response term due to the single-component STF, six bilinear-response terms, nine third-order response terms due to the single-STF and single-SLF-component couplings, and 12 trilinear-response terms. We see that the prediction is accurate for smaller force amplitudes, but it is less accurate for the largest force amplitudes, especially in the regions

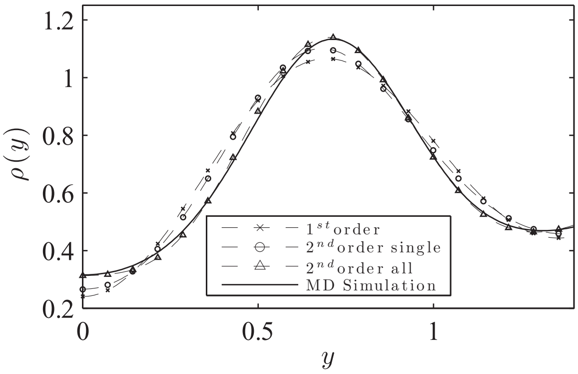

FIG. 12. Convergence of the truncated expansion density profile toward the MD density profile for a three-component SLF. Magnification of the first peak in Fig. 11 for $F_6^y = F_8^y = F_{10}^y = 2.5$. The thick line represents the MD density. Thin dashed lines indicated with symbols represent different orders of truncation.

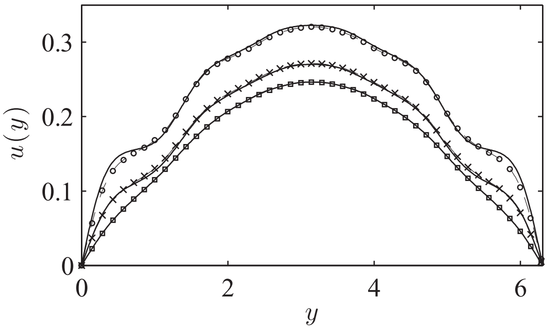

FIG. 13. Comparison between velocity profiles obtained directly from MD simulations and predictions of the truncated functional expansion using independently calculated response functions for single-component STF and three-component SLFs. Bold lines represent MD simulations, thin dashed lines with symbols represent predictions. The system parameter labels are the same as those used in Fig. 11. Velocity profiles only shown for half of a wave cycle.

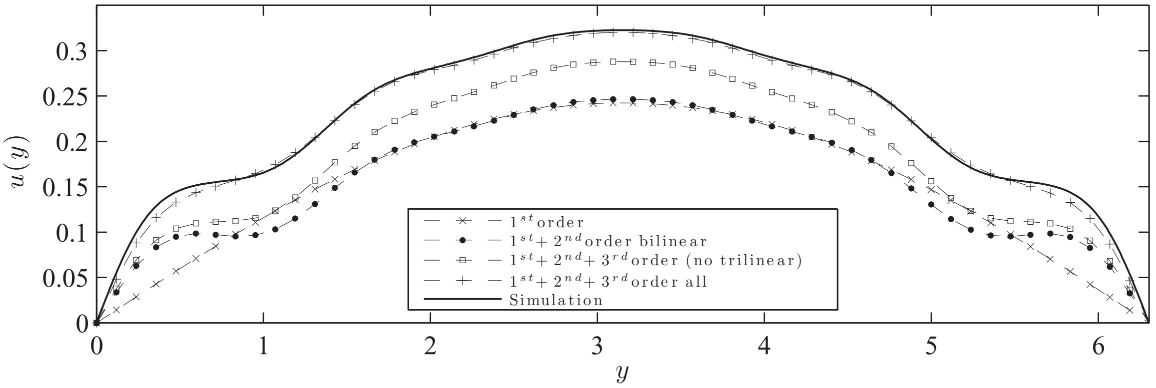

FIG. 14. Convergence of the predicted velocity profile toward the MD simulation velocity profile for a single-component STF and a three-component SLF. $F_1^x = 0.08$ and $F_6^y = F_8^y = F_{10}^y = 2.5$. Velocity profiles only shown for half of a wave cycle.

where the density perturbations are greatest. Note that the resulting field is extremely large with a combined force amplitude of $F_6^y + F_8^y + F_{10}^y = 7.5$. Third-order effects are expected to be observed at these field strengths [15]. The convergence plot shown in Fig. 14 confirms the similarity with the two-component SLF system shown in Fig. 8. It shows that the oscillatory behavior is predominantly due to the bilinear response described in Ref. [17]. It also shows that there is no significant error in the fundamental velocity component. This means that the contributions to the fundamental component are from sources previously discussed and that there is no additional contribution from, for example, a four force component coupling. This is an encouraging result. It should be kept in mind, however, that for some other combinations of m_1,m_2,m_3 we may find excitations at the fundamental velocity component. We now have five third-order contributions to the fundamental velocity component: $\xi^{xyy0}_{1,6,6}$, $\xi^{xyy0}_{1,8,8}$, $\xi^{xyy0}_{1,10,10}$, $\xi^{xyy--}_{1,6,8}$, and $\xi^{xyy--}_{1,8,10}$. Given that there are so many contributions to the velocity at this wavelength, it is a testament to the accuracy of the method that there is so little error in this component of the velocity.

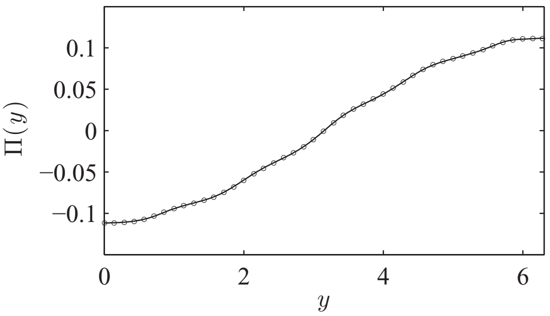

FIG. 15. Comparison between shear-pressure profiles obtained directly from MD simulations and the truncated functional expansion prediction using independently computed response functions for a single-component STF and a three-component SLF. Bold lines show MD simulations, thin dashed lines indicated with symbols show predictions. $F_1^x = 0.08$ and $F_6^y = F_8^y = F_{10}^y = 0.5$, 1.5, and 2.5. Shear pressure profiles only shown for half of a wave cycle.

C. Shear pressure

Finally, we consider the shear-pressure profiles for fluids under a single-component STF and a three-component SLF. In Fig. 15, we show the shear-pressure profile for one particular system. The Fourier series expansion will have the same set of terms as the velocity profile, except that three of the third-order response terms due to the single-STF and single-SLF-component couplings will not be included since, as has been discussed, there is no third-order contribution to the fundamental shear-pressure component. We show only the case of $F_1^x = 0.08$ and the largest SLF amplitudes, i.e., $F_6^y = F_8^y = F_{10}^y = 2.5$. The prediction and the simulation are in excellent agreement.

VII. CONCLUSIONS

We have investigated the density, velocity, and shear-pressure profiles of a fluid under the influence of a single sinusoidal transverse force and a multiple-component sinusoidal longitudinal force. We have extended a method that we introduced in a previous publication, where we used only single sinusoidal transverse and longitudinal forces in combination to calculate various nonlocal response functions describing the formation of the density, strain rate, and shear-pressure profiles in simple atomic fluids. There are two reasons for extending the treatment to multicomponent SLFs in this publication. First, we wish to determine the nature of the density response to external fields that are more complex than single Fourier component external fields. This is helpful when we consider that the effects of a solid wall on a fluid at a fluid-solid interface can be represented as an effective external field that is much more complex than a single Fourier component external field. Second, the extension to multicomponent SLF systems has allowed us to generalize our description of the coupling between the transverse and longitudinal forces to include more complicated longitudinal forces. Again, this knowledge will be very helpful when considering the coupling relationships that are known to occur in flowing, nanoconfined fluids, where the density profiles due to the fluid-solid interface are quite complex. Therefore, this extension to multicomponent SLFs helps us to determine which orders of response are important when describing strongly inhomogeneous shearing fluids and which orders of coupling significantly effect the fluid properties.

We have shown that for each pair of SLF components used in superposition, we excite two additional harmonics in the density profile due to bilinear coupling. By evaluating the amplitudes of these density harmonics, we have shown that we can calculate two bilinear density response functions, which are two-dimensional in Fourier space. Using single-component SLFs, we can only access a one-dimensional slice of one of these functions, which is necessarily equivalent to the second-order density response function discussed in [15,17]. We have shown that these additional bilinear-response terms provide a significant contribution to the total density profile, and so it is necessary to include this lowest-order coupling relationship when describing the density response to external fields. We have also shown that for each combination of a single-component STF and a two-component SLF, we excite four additional harmonics in the velocity profile and four additional harmonics in the shear-pressure profile. These harmonics depend linearly on each force amplitude. We have evaluated the Fourier coefficients for four additional third-order response functions for both the strain-rate response and the shear-pressure response, and we have considered the relative contributions of different terms, showing that some are indeed significant, especially those that influence the fundamental components of the strain rate and shear pressure. Other terms are negligible.

We have predicted density, velocity, and shear-pressure profiles for various combinations of a single-component STF and two-component SLFs. Our predictions are generally in excellent agreement with profiles directly calculated using MD simulations. For the density profiles, we required very large force amplitudes to see a significant difference between the predicted profile and the MD profile. It is most likely that the small differences observed were due to our exclusion of third- and higher-order density response terms.

For the velocity profiles, we confirmed that most of the short-wavelength oscillatory behavior is due to the second-order bilinear response, as was discussed in [17]. We showed that the velocity profile is greatly affected by multiple third-order contributions to the fundamental velocity component. In many instances, we found that there were significant contributions to the fundamental velocity component from the additional third-order terms. In general, these terms could not be neglected, but in some cases, such as for short-wavelength contributions, we could neglect these additional third-order terms. For the shear pressure, we have shown that including third-order terms does slightly increase the accuracy of the predictions, but the profiles are already well described by the linear and bilinear response. Many of the third-order contributions to the shear pressure could be neglected.

Finally, we showed that it is possible to accurately describe fluids that are perturbed by a single-component STF and a three-component SLF without needing to account for any four force component couplings. The success of this approximation shows that there is a limit to how many orders of coupling we need to account for as we add more SLF components. It would appear that it is sufficient to only account for at most the coupling between each single STF and each pair of SLF components. This result paves the way for describing shearing fluids with inhomogeneous density profiles using functional expansions truncated at the second-order response in the density and third-order response in the velocity and shear pressure. This is a very promising result for the prediction of flow in fluids under the influence of complex external fields, and possibly even hard walls.

Overall, we can conclude that the integral-type constitutive relations that we have proposed can fully account for both nonlocality and coupling in systems with flow and density inhomogeneities on molecular length scales. This is likely to be true, not only for the simple fluid that we have investigated, but also for any dense fluid having a structure that is dominated by its hard-core interactions. The response functions that we have introduced should be useful for predicting density, velocity, and stress profiles in highly confined flows where density inhomogeneity and its coupling to the velocity profile are important factors.

ACKNOWLEDGMENTS

This work was supported by the Australian Research Council through the Discovery-Projects scheme, project ID DP120102976. We thank the Victorian Partnership for Advanced Computing for the use of their facilities. B.D. would like to thank the Australian government for their support through an Australian Postgraduate Award.

---

[1] W. Sparreboom, A. van den Berg, and J. Eijkel, New J. Phys. **12**, 015004 (2010).

[2] R. Qiao and N. Aluru, J. Chem. Phys. **118**, 4692 (2003).

[3] R. Nilson and S. Griffiths, J. Chem. Phys. **125**, 164510 (2006).

[4] B. D. Todd, J. S. Hansen, and P. J. Daivis, Phys. Rev. Lett. **100**, 195901 (2008).

[5] I. Bitsanis, J. J. Magda, M. Tirrell, and H. T. Davis, J. Chem. Phys. **87**, 1733 (1987).

[6] J. S. Hansen, J. C. Dyre, P. J. Daivis, B. D. Todd, and H. Bruus, Phys. Rev. E **84**, 036311 (2011).

[7] I. Bitsanis, T. K. Vanderlick, M. Tirrell, and H. T. Davis, J. Chem. Phys. **89**, 3152 (1988).

[8] I. K. Snook and D. Henderson, J. Chem. Phys. **68**, 2134 (1978).

[9] I. K. Snook and W. van Megen, J. Chem. Phys. **70**, 3099 (1979).

[10] F. F. Abraham, J. Chem. Phys **68**, 3713 (1978).

[11] S. Toxvaerd, J. Chem. Phys. **74**, 1998 (1981).

[12] B. D. Todd, D. J. Evans, and P. J. Daivis, Phys. Rev. E **52**, 1627 (1995).

[13] K. P. Travis and K. E. Gubbins, J. Chem. Phys. **112**, 1984 (2000).

[14] L. Pozhar and K. E. Gubbins, J. Chem. Phys. **99**, 8970 (1993).

[15] B. A. Dalton, K. S. Glavatskiy, P. J. Daivis, B. D. Todd, and I. K. Snook, J. Chem. Phys. **139**, 044510 (2013).

[16] B. A. Dalton, P. J. Daivis, J. S. Hansen, and B. D. Todd, Phys. Rev. E **88**, 052143 (2013).

[17] K. S. Glavatskiy, B. A. Dalton, P. J. Daivis, and B. D. Todd, Phys. Rev. E **91**, 062132 (2015).

[18] J. P. Hansen and I. R. McDonald, *Theory of Simple Liquids* (Academic Press, London, 2006).
[19] S. Nosé, Mol. Phys. **52**, 255 (1984).
[20] S. Nosé, J. Chem. Phys. **81**, 511 (1984).
[21] W. G. Hoover, Phys. Rev. A **31**, 1695 (1985).
[22] B. D. Todd and P. J. Daivis, Mol. Sim. **33**, 189 (2007).
[23] A. Baranyai, D. J. Evans, and P. J. Daivis, Phys. Rev. A **46**, 7593 (1992).
[24] K. P. Travis, D. J. Searles, and D. J. Evans, Mol. Phys. **97**, 415 (1999).
[25] J. S. Hansen, P. J. Daivis, K. P. Travis, and B. D. Todd, Phys. Rev. E **76**, 041121 (2007).